Multimedia Tools and Applications (2021) 80:3017–3037
https://doi.org/10.1007/s11042-020-09797-3

Content-based image retrieval algorithm for nuclei segmentation in histopathology images

CBIR algorithm for histopathology image segmentation

Yashwant Kurmi[1] · **Vijayshri Chaurasia**[2]

Received: 21 July 2019 / Revised: 27 August 2020 / Accepted: 2 September 2020 /
Published online: 18 September 2020

Abstract
In today's world, the medical diagnostic system shows a high reliance on medical imagery and digital nosology. To facilitate the fast and precise screening of samples, technology is leading towards the computer-aided disease diagnosis and grading. Image segmentation possesses high worth in the computer-aided disease diagnosis and grading systems to extract the region of interest. This paper presents a content-based image retrieval algorithm for histopathology image segmentation for identification and extraction of nuclei. The proposed technique furnishes nuclei segmentation in three cascaded stages; pre-processing, nuclei points and region refining, and composite nuclei segmentation. The performance of nuclei segmentation is investigated on six hematoxylins and eosin (H&E) stained histopathology images datasets. Simulation outcomes of the segmentation schemes confirm the superiority of the proposed method for nuclei segmentation in histopathology images in qualitative and quantitative analysis.

Keywords Histopathology images · Microscopic image segmentation · Contour enhancement · Content-based image retrieval (CBIR) · Nuclei segmentation

1 Introduction

Image segmentation be classified among important processes in the image analysis to emphasize the target area. In the nosology field, image exploration plays an important role in the diagnosis and prognosis of diseases. The research work in various fields of medical imaging is going on to make a perfect diagnosis. Lots of research is going on in the medical

✉ Yashwant Kurmi
yashwantkurmi18@gmail.com

Vijayshri Chaurasia
vchaurasia@manit.ac.in

[1] Maulana Azad National Institute of Technology, Bhopal, 462003, India

[2] Electronics and Communication Engineering Department, Maulana Azad National Institute of Technology, Bhopal, 462003, India

imaging field to develop a standardized, quantified, and reproducible system for computer-aided diagnosis (CAD) [23, 27]. In the segmentation routine, firstly, the seed/key points are extracted to mark the object of interest in the preprocessed image. The tissue deformation study at the microscopic level is termed as histopathology. The captured image at the microscopic level is characterized by histopathology images [HI]. Image preprocessing is an obligatory step in case of a large dataset to transform images of diverse sources to the same platform and provide a single image analysis method for their processing. A preprocessing method provides a compatible solution to process these image varieties by a single image analysis method. The preprocessing may be applied in the form of chromatin morphology, color normalization, and transformation [22] to make suitable images for further analysis.

The seed points were extricated using key realm enhancers as a kernel mapping and/or Laplacian of Gaussian filter application [18, 26] and utility of Gaussian mixture model (GMM) for pixel-level clustering [15]. A kernel application [25] is a good practice to map the image in a high dimensional Hilbert space for the ease of region separation. The transformed high dimensional map provides a peak/valley point corresponding to the object, subject to the constraints of the selected image. The next step is the region of interest segmentation also called image binarization may consider a graph-cuts method [1], and active contours [2, 16] focused on key points. The overlap resolution of objects is an issue in efficient segmentation and is investigated using concavity detection and geometric reasoning in [41] and [48] respectively.

The segmentation performance of existing methods is database reliant and offers efficacious results for a specific set of data. The proposed kernel-based method is basically focused to segment the nuclei in histopathology images. The method is developed to segment the most possible image categories of nuclei. The proposed method contains the following steps: the first step is to enhance the image contrast for the nuclei using a preprocessing [6] [39] by the histogram equalization and proposed object size kernel application [52]. The 2-D circular kernel function provides a peak/valley points of nuclei at their centers. It basically provides the initial points for nuclei detection. In the next step, multi-thresholding [28, 55] was applied to obtain the over-segmented region and it was further refined using an active contour application [3, 5]. An iterative morphological erosion [20] was applied to shrink the nuclei boundary and easy to get the point level marking of nuclei. The nuclei center points were extracted using ultimate erosion [21] by considering the nuclei radius as a constraint. Serra and Matheron worked a lot on the morphological operators and provided a new domain of mathematical morphology [19]. The nuclei region boundary was extracted by applying the canny edge detector [4] and discrete morphological edge thinning [30]. The contour to nuclei points association [62] was performed by locating the nearest boundary to the selected nuclei center point. The selected center point and its nearest best suitable boundary were utilized for ellipse fitting [40] in the final step.

The contribution of this paper is the kernel design and the nuclei points refinement process to deal with the complex boundary nuclei segmentation using the radius of nuclei as constraints. We analyze the performance of our method by utilizing five existing datasets for the segmentation of nuclei region. The kernel limitation is that it performs poorly in the case of multiple overlap nuclei cases (very big clusters). The kernel works in the objects' radius equivalent or less than the kernel size. We also proposed a multi-organ histopathology image dataset of 12 patients and analyzed it. The successful segmentation for the cases that detects at least 80% of the nuclei have an average Dice coefficient 0.6.

The next section describes the detailed literature survey followed by the proposed segmentation methodology described in Section 3. Section 4 explains the concrete experimental

results and discussion comparison with the state of art techniques. Lastly, Section 5 encapsulates the conclusions of the paper.

2 Literature review

The image segmentation techniques have a wide diversity in the field, some of the related techniques are discussed here. The tissue texture and spatial structure-based-details [47] were utilized to resolve the boundary overlapping of nuclei. Wang et al. [57] presented a chromatin morphology-based cell characterization through an optimal transportation matrix (Kantorovich Wasserstein) [60] that measures the relevant biological information. The nuclei distributions and differences were computed by utilizing Fisher discriminant analysis [56] along with multidimensional scaling applied to optimal transportation distance map [57]. Large computational cost was the major issue of this methodology. Dundar et al. [15], have segmented the cell region through the GMM-based pixel clustering followed by a watershed algorithm. Cell region was segmented through the GMM-based pixel clustering and the individual cells were segmented by utilizing watershed-based segmentation.

Ali et al. [2] and Chang et al. [6] were presented a priors representation using GMM and color normalization [59], color transformation, and scale information based-feature extraction along with multi-reference-based background and foreground separation. Zafari et al. presented [62] an algorithm as Bounded erosion followed by the Fast radial symmetrical transform and Contour assessment (BFC) for overlapping objects segmentation. Wang worked on a semi-automatic method (SAM) [55] based on alternative threshold computation and morphological operations. Nuclei's portrayal of overlapped objects was resolute by detecting concavities and partitioned them through geometric syllogism [49]. Chowdhary et al. [9] analyzed an intuitionistic possibilistic fuzzy c-mean (FCM) approach [7, 8, 10–12]. Lei et al. [37] improvised the FCM algorithm through morphological redintegration and membership filtration (FRFCM). These algorithms clutch the constructive points of the considered model to overcome the concomitant cluster problem by diminishing the noise effect with outliers sensitivity reduction and preserving image details.

Peng et al. [45] presented a local mean as well as variance based-active contouring (LVMAC) approach to segment the medical images through the Gaussian dispersal. Vu et al. [54] presented the nuclei segmentation system as well as the whole slide classification approach. The segmentation procedure implements a multiscale deep residual aggregation network (MDRAN) for segmenting the nuclear region followed by clamped nuclei separation. The classification setup initially, based on patch level using deep learning and further extended to whole-slide image classification using statistical and morphological properties as input to a random forest regressor. Yu et al. [61] worked on a pyramidal facet adaptation based semi-supervised system (PABVS) to segment the cardiac bi-ventricle. Initially, it employed the multiscale pyramidal characteristics of bi-ventricle shape and then adversarial learning based on level-wise weighted feature adaptation to manage its high variability and less sensitive to outliers.

Sheela et al. [46] combined the prior knowledge of a specified region, seen growing, as well as morphological functioning (dilation and erosion). The FCM clustering, followed by base structure realm growing (FCMRG) has been utilized for detecting and segmenting the region of interest in the image. Vargas et al. [42] modified the FCM clustering algorithm in terms of the robust statistics to develop an iterative image segmentation method using color features. The non-parametric Lorentzian Redescending M-estimator was utilized in

the clustering algorithm; since its working is as location estimator to compute the centroid vector and at the time of the membership matrix update it acts as a weighting matrix.

Zhao et al. [64] combined the image refinement process to investigate the imaging system and enhance the image lucidity. It processes the stereotype data by image computation process to obtain noticeable statistical image features [11, 33]. Dhanachandra et al. [43] also utilized a combined process of dynamic particle swarm optimization (DPSO) with the FCM that utilized the beneficial points of the globally optimized searching process and parallel computation of DPSO for image enhancement and segmentation. Kim et al. [29] presented an unsupervised image segmentation system that used an argmax function after normalization for differentiable clustering. After that, a spatial continuity loss function was utilized to eliminate the limitations of the segmented region edges. Lei et al. [38] investigated a fingerprint segmentation approach using an FCM and genetic algorithm that was relying on the gray level present in image and post-processing steps.

Sun et al. [53] applied the existing convolutional neural networks (CNNs) and presented a hierarchical conditional random field (HCRF) based approach for gastric histopathology image segmentation that localize the cancer regions in HIs. Xia et al. [58] applied the FCM clustering approach to segment the image at a global level for shape properties extraction and region of interest identification. It improvises the clustering robustness and offers the trade-off between smoothening and high-frequency information preservation through fine-tuning using the soft voting technique. The limitations of these methods are directly processing the images for classification of pixels to segment that limits the segmentation accuracy. The mentioned problem is resolved by the proposed method using the preprocessing, refinement, and specific region identification and complex nuclei separation.

3 Proposed segmentation method

The content-based image retrieval (CBIR) algorithm for nuclei segmentation uses the prior knowledge of the histopathology images. The complete proposal of HI segmentation is defined in three cascaded steps; A) preprocessing, B) nuclei points and region refinement, and C) complex nuclei segmentation. The flowchart of the proposed segmentation technique is depicted in Fig. 1.

3.1 Preprocessing

The nuclei region enhancement as preprocessing in the proposed technique is accomplished by histogram equalization followed by the application of object size kernel. Firstly, the histogram equalization is applied with the computational complexity of $O(L^2)$ where L is the total number of intensity levels.

The specified size kernel (W) is adaptively fabricated using the radius of approximated nuclei. Lets consider R is the radius of the defined object. The radius of circular kernel (W) is taken equal to the diameter of considered object as presented in [36]. The kernel design structure with a 3-D visual illustration of application on histogram equalized image is shown in Fig. 2.

The elementary form of kernel design is described through the pseudo-code in Algorithm 1. The computational complexity in kernel design is $O(D^2R)$. The processed image after kernel application is I_F as

$$I_F = I_H * W \tag{1}$$

where asterisk symbol * represents convolution function between image I_H and kernel W as shown in Fig. 2.

Algorithm 1 Pseudocode of kernel design.

Input: Radius r
Output: Normalized kernel MW_1

Step 1 Initialize
$D_k \leftarrow$2*r+1; specified object size
W $\leftarrow$zeros(D_k, D_k); initialize zero matrix of size $D_k \times D_k$
W(r,r)$\leftarrow$255; assign 255 to central elements of size r×r
$W_1 \leftarrow$W; take another variable of size W
Step 2
For $i = 1$ to $r/2$ **do**
$W_1 \leftarrow$ imdilate(W_1)
Radius: rd$\leftarrow$(W $\neq 0$); $rd_1 \leftarrow (W_1 \neq 0)$
$W_2 \leftarrow$ imrotate(W_1, θ); if r ≤ 5, θ =30; else θ =45
$W_3 \leftarrow W_2(rd + 1 : rd_1, rd + 1 : rd_1)$;
$W_1 \leftarrow W_1 + W_3$; $W_1 \leftarrow (W_1 \neq 0)\ 255$
End For
Step 3
Sum: $SW_1 \leftarrow \sum_{i=1}^{M} \sum_{j=1}^{N} (W_1(i, j))$; Edge: Ed$\leftarrow$[.]
For $i = 1$ to $r/2$ **do**
If i==1
$MW_1 \leftarrow$ imdilate(W_1, strel('disk',1)) ;Ed $\leftarrow MW_1 - W_1$;
Sum: SEd= $\leftarrow \sum_{i=1}^{M} \sum_{j=1}^{N} (Ed(i, j))$ (a)
Opposite Values (OV) $\leftarrow SW_1 \div$ ((r/2)*SEd) (b)
Ed $\leftarrow$ -OV; $W_2 = W_2 + Ed$; (c)
Else
$MW_1' \leftarrow$ imdilate(MW_1, strel('disk',1))
Ed $\leftarrow MW_1' - MW_1$;
Repeat steps (a)-(c).
$MW_1 = MW_1'$
End If
End For
End

Note:
imdilate shows the dilation operation on matrix or image.
imrotate command rotate the image with specified angle.
strel represents the morphological structuring element.

In the tissue, nuclei are surrounded by different types of components and possess different types of relationships with the surrounding in various locations of the entire HI. Due to this, the selection of any specific value for the identification of nuclei and the non-nuclei region is very difficult. In the proposed segmentation method, nuclei region extraction is performed by a combination of the Otsu threshold [44] and the discrete cosine transform (DCT) based threshold selection methods [28]. The Otsu's thresholding method has the computational complexity of $O(L^2)$ like histogram equalization. The amended threshold (T_1) using Otsu threshold (T) is computed by the following relations:

$$T_1 = (1 + T_\alpha) * T \tag{2}$$

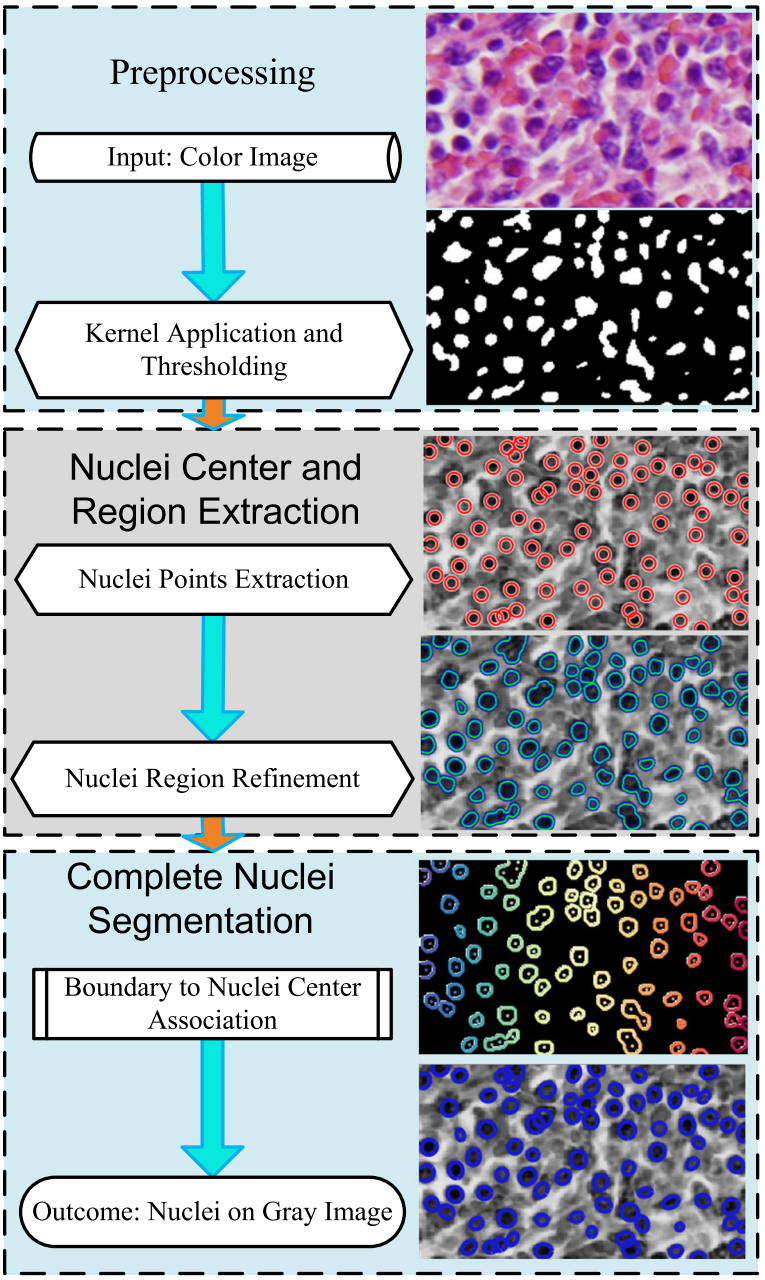

Fig. 1 Flowchart of the proposed method

where T_α is threshold normalization parameter which ranges between 0.08 to 0.22. The value of T_α is directly proportional to the mean intensity of image. T_2 is obtained using DCT based thresholding method [28].

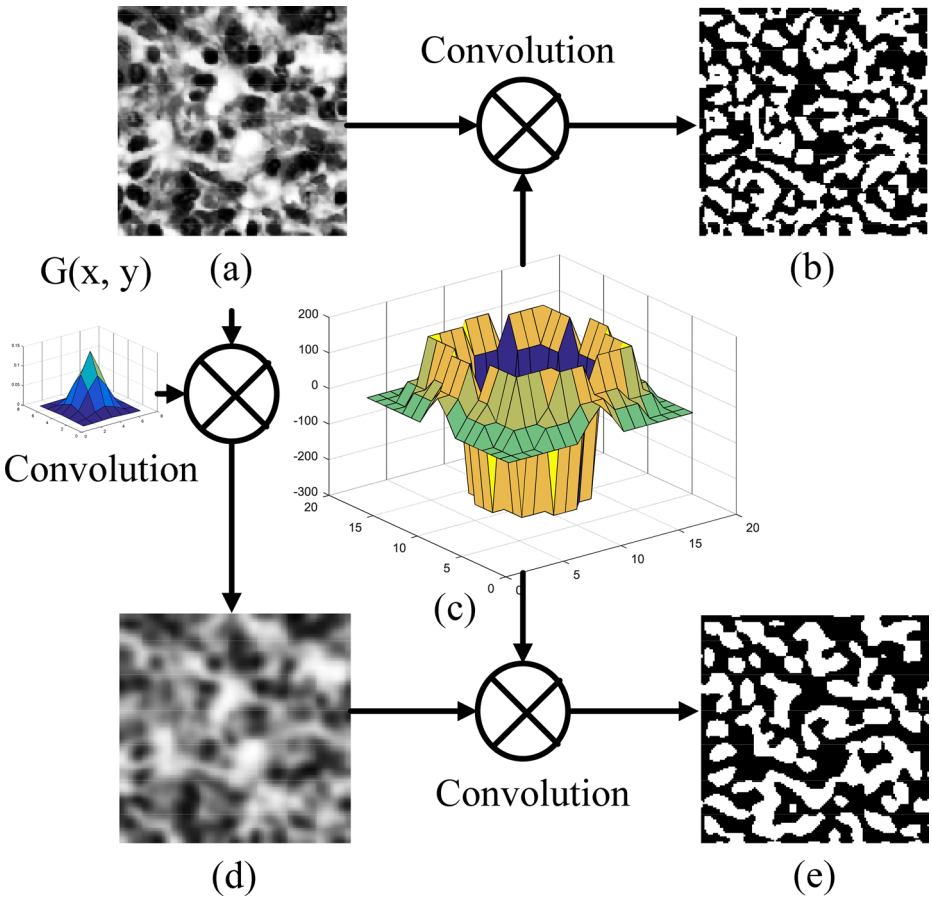

Fig. 2 **a** Histogram equalized image **b** the outcome of kernel application on (a), **c** object size kernel **d** smooth image by Gaussian filtering **e** the resulting image by applying the kernel on the smoothen image

Two segmented images using thresholds T_1 and T_2 are combined to form an initialization mask for nuclei boundary extraction. This mask creation reduces the search space for the subsequent processing steps. In other words, let the binary initialization mask is I_M and it is obtained by the following relation

$$I_M = \begin{cases} 1; & I_F \leq T_b \\ 0; & I_F > T_b \end{cases} \tag{3}$$

where $T_b = max(T_1, T_2)$ is the overall threshold. I_M will further be processed for the nuclei boundary using local region energy-based contours to get an energy-optimized image (I_{EO}).

3.2 Nuclei center and region extraction

The existence of overlapping and touching nuclei results in false identification in nuclei boundary extraction. To resolve this issue, nuclei center points are identified using iterative morphological erosion and used as seed points for segmentation. The pseudo-code for nuclei points refinement is explained in Algorithm 2.

Algorithm 2 Nuclei center extraction.

Input: Radius r, D= 2r, separation distance d=0.75D,
Seed image
Output: Overlapped nuclei resolved points

Step 1 E← Mx2 matrix of x and y coordinates of the seed point
Step 2 X coordinates Ex ← E(:,1); Y coordinates Ey ←E(:,2);
Step 3 Repeat each coordinate to form a square matrix
ExRep = repmat(Ex, 1, length(Ex));
EyRep = repmat(Ey, 1, length(Ey));

Step 4 Calculate the distance between every set of points
dX = ExRep - ExRep'; dY = EyRep - EyRep';
distAll = $\sqrt{dX^2 + dY^2}$;

Step 5 Seed points that are at less then distance d
smallDist = distAll < d;
Step 6 If smallDist ≤ r/2
The centroid of these points becomes center

Step 7 Else if r/2 < smallDist < d & number of points < 4
Extremes becomes the seeds center points

Step 8 Else r/2 < smallDist < d & number of points ≥ 4
Extremes and centroid becomes the seeds center points

Step 9 Repeat steps 3-8 until overlapped cases resolved
End If
End

Note:
repmat repeats the considered elements to specified dimension.

Let $\Omega \subset \mathbb{R}^d$ and $f : \Omega \to \mathbb{R}$ is an image of d-dimension. The B-spline (BSP) level-set function has an interface $\Gamma \subset \mathbb{R}^d$ represented in terms of an implicit boundary function $\phi(.)$ at the zero level-set. It is a linear combination of BSP basis functions [3] is given as

$$\phi(x) = \sum_{k \in mathbb(Z)^d} [c[k]]\beta^n(\frac{h}{x} - k) \tag{4}$$

Here the BSP function $\beta^n(.)$ is the symmetric d-dimensional having the degree n. The knots or cross points of the BSP can be marked using a grid spanning Ω, at a regular interval. The measures of the BSP rendering are accumulated in $c[k]$. The parameter h has a scale value that controls the smoothness of the interface. The suitable energy function is defined by the following equation

$$E(\phi) = \int_{\Omega} F(I(x), \phi(x))dx, \tag{5}$$

To implement the proposed segmentation problem the value of F is computed from the Chan & Vese data analysis as

$$F(I(x), \phi(x)) = H(\phi(x))(I(x) - v)^2 + (1 - H(\phi(x)))(I(x) - u)^2 \tag{6}$$

Here H is a well known Heaviside function and the update parameters u and v are used at each iteration as per the (7) and (8).

$$u = \frac{\int_{\Omega_{x'}} (1 - H\phi(x')).I_{x'}dx'}{\int_{\Omega_{x'}} (1 - H\phi(x'))dx'} \tag{7}$$

$$v = \frac{\int_{\Omega_{x'}} H\phi(x').I_{x'}dx'}{\int_{\Omega_{x'}} H\phi(x')dx'} \tag{8}$$

The minimization of the functional (5) can be done using the BSP parameters $c[\mathbf{k}]$. The derivatives of energy function with respect to every BSP functional parameter $c[\mathbf{k}_0]$ is defined as

$$\frac{\delta E}{\delta c[\mathbf{k}_0]} = \int_{\Omega} \frac{\delta F(x, \phi(x))}{\delta \phi(x)} . \beta^n (\frac{x}{h} - \mathbf{k}_0) dx \tag{9}$$

with

$$\frac{\delta F(x, \phi(x))}{\delta \phi(x)} = \delta\phi(x)(I(x) - v)^2 - (I(x) - u)^2 \tag{10}$$

The evaluation of the level-set function was computed using the gradient descent of the BSP functional parameters. The respective variation in the BSP parameters is depicted as:

$$c^{i+1} = c^i - \lambda \nabla_c E(c^i) \tag{11}$$

where parameter λ represents an iteration number and ∇_c shows the energy gradient of the BSP parameters given by (9). The smoothness parameter h is a scalar integer number to represents the degree of smoothness of contour ($h \leq 4$).

3.3 Complete nuclei segmentation

The image formed after application of nuclei center and region extraction is further processed for complex nuclei identification using the center to boundary association with curve fitting.

3.3.1 Nuclei boundary extraction

The nuclei region boundary was extracted by applying the canny edge detector on I_{CF} followed by discrete morphological edge thinning.

3.3.2 Nuclei boundary and center point association

The nuclei border contour to center point association was performed by locating the nearest boundary pixels to the selected nuclei center. It combines the distance with divergence rate to assign the boundary pixels to a center point. The elementary-code for boundary extraction is given in Algorithm 3.

Given a set of nuclei center points $C = \{c_1, c_2, ..., c_n\}$, every boundary pixels b_k in $B = \{b_1, b_2, ..., b_m\}$ represents a relation to the identified nuclei center points using a relevancy metric $rel(b_k, c_j)$ given by

$$rel(b_k, c_j) = \frac{1 - \lambda}{1 + dist(b_k, c_j)} + \lambda \frac{div(b_k, c_j) + 1}{2} \tag{12}$$

where $dist(b_k, c_j)$ and $div(b_k, c_j)$ are the Euclidean distance and divergence functions, respectively. These values are normalized in the range (0,1] and then added through the weight λ. By using the above relation, the boundary pixel b_k is assigned to center point c_j with optimum relevancy. The function $dist(b_k, c_j)$ represents the distance from boundary point b_k to the nearest center point c_j. The assumption is taken for all the pixel values on the connecting line of boundary points to center point $l(b_k, c_j)$ considered as nuclei region M:

Algorithm 3 Nuclei boundary extraction and center point association.

Input: Grayscale image I, Divergence factor λ [0-1]
and circular search radius r,
Output: Center-boundary associated nuclei

Step 1 Gradmag←Gradient(I) = canny-edge(I)

Step 2 Thinning the edge points using 'bwmorph' command:
Gradmag ← bwmorph(Gradmag)

Step 3 To minimize complexity take alternate edge points

Step 4 Edge points [nmepnts]← find(Gradmag)

Step 5 Seed points nmspnts ← length(seedpoints)

Initialize *For* loop up to nmspnts

Step 6 Iterate over seedpoints in search regions: XYEI

Step 7 Compute distance seed points to edges: EG

Step 8 Estimate divergence for seed region 'xysr'
dvg = cmpdivergence(xysr, XYEI, dy, dx)

Step 9 Compute relevance

Step 10 rel1 = 1./(1+EG);
rel2 = (dvg+1)/2; rel2(rel1==0) = 0;
rel = (1-λ)*rel1 + λ*rel2;

Step 11 Assign edge XYEI to seedpoint with the highest
relevance value

relmax, idxrm ← max(rel)
Edge2SeedpointAsso ← idsr(idxrm) (Using a linear index)

End *For* loop

End

The computation of gradient on a given point x is

$$g(x) = \begin{cases} \|b_k - c_j\|; & if(b_k,\ c_j) \subset \mathbf{M} \\ \infty; & otherwise \end{cases} \tag{13}$$

The function $div(b_k, c_j)$ shows the difference of directions between the line connecting the boundary point b_k to center point c_j and gradient direction at boundary point b_k, and is computed by taking cosine of the angle between them:

$$div(b_k\ c_j) = \frac{g(b_k)l(b_k,\ c_j)}{||g(b_k)||.||l(b_k,\ c_j)||} \tag{14}$$

The computational complexity for the boundary to seed point association is $O(N^2 N_p L_B)$. To reduce the number of latent false classified boundary points and the computational cost, the region was searched adaptively in the circular expanse near every boundary point individually so that fewer center points were processed. After defining a circular zone and taking the alternating boundary points the computational complexity for the boundary to seed point association is $O(N^2 L_B/2)$. Figure 3 demonstrates the boundary-to-center point association to estimate boundary evidence. The red arrow shows the direction of the gradient at boundary point b_1, the dashed arrows of black and blue color show the direction of the lines connecting b_1 to c_1 and c_2 respectively.

3.3.3 Complex nuclei identification

Once the contour evidence has been determined, the boundary estimation is performed to predict the missing region of the nuclei. The contour estimation was addressed to model the partially visual nuclei through an ellipse fitting [62], [17]. The elementary-code for complex nuclei identification is explicated in Algorithm 4.

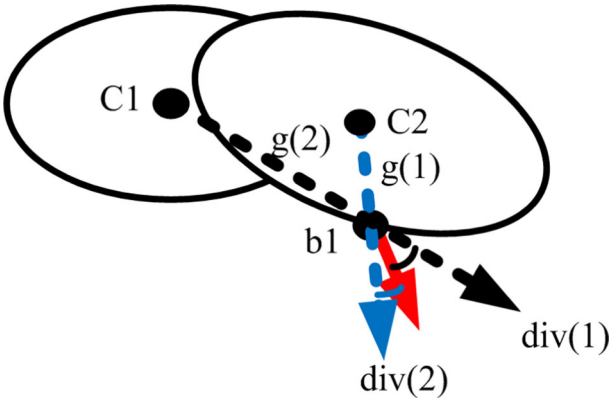

Fig. 3 Illustrative example of boundary to center point association. The boundary point b_1 near to C_2 has more weight (high divergence value) for $b_1 - C_2$ association and less weight for $b_1 - C_1$ and by comparing the distance ($g(1)$ and $g(2)$) and divergence values ($div(1)$ and $div(2)$). $g(1) < g(2)$ and $div(2) > div(1)$. Both the parameters supports as b_1 is the boundary point of C_2

Algorithm 4 Complex nuclei segmentation.

Input: Input: Image I, Edge2SeedpointAssoc, and
A constraint matrix of dimension 6x6
C(6,6) = 0; C(1,3) = -2; C(2,2) = 1; C(3,1) = -2
Output: Ellipse plot using (X,Y) coordinates for
overlapped nuclei region

Step 1 Initialize *For* loop-1 up to number of Seed points

Step 2 Normalize data
x ← (X-mean(X))/(max(X)-min(X)/2
x' ← (X'-mean(X'))/(max(X')-min(X')/2

Step 3 Make matrix $D = \left[x^2 \; xx' \; x'^2 \; x \; x' \; 1\right]$
Step 4 Scatter matrix S ← D'*D
Step 5 Find eigen values and eigen vectors
Evec, Eval ← eig(S,C)

Step 6 Find eigenvector corresponding to negative
eigenvalue A = Evec(Eval<0)
Step 7 Unnormalize A

Step 8 From A compute the ellipse parameters
v ← Major and minor axis, x-center, y-center, and θ

Step 9 Find ellipse boundary with N=50 points, θ = v(5),
and $R = \begin{bmatrix} cos(\theta)sin(\theta) \\ -sin(\theta)cos(\theta) \end{bmatrix}$

Initialize *For* loop-2 up to N points

Step 10 $\theta = 2\pi$/N ×loop-number
x = v(1) ×cos(θ); y = v(2) ×sin(θ);
X= R.x +v(3); Y= R.y +v(4)

Step 11 Output: Ellipse plot using (X,Y) coordinates

End *For* loop-2
End *For* loop-1
End

4 Result and discussion

Performance evaluation of the proffered HI discrimination technique is done using five existing HI datasets and one proposed multi-organ dataset; 1) Animal Diagnostics Lab

(ADL) dataset [51], 2) Bisque dataset 3) Nuclei dataset by A. Janowczyk [24], 4) BreaKHis dataset [50], 5) MICCAI 2018 [31], and 6) Dataset prepared by us in association with All India Institute of Medical Sciences (AIIMS) Bhopal India, and Jawaharlal-Nehru Cancer-Hospital & Research-Center (JNCH&RC), Bhopal, India [34, 36]. The detailed information of the proposed dataset is given in the supplementary material provided with the manuscript. The experiments on 60 images taken from six different datasets are performed for the quantitative assessment. The parameters used for evaluation measures are discussed in Section 4.1. The experiment with different kernel radius was performed to get the optimum value for the best performance of the proposed method in consecutive subsection.

4.1 Evaluation measures

There are four existing evaluation measures used for validation of the proposed method. F_1-score (FS), [32], Dice similarity coefficient (DC) [13], and modified Hausdorff distance (MHD) [14, 35]. Accuracy is the most intuitive measure for analyzing classifiers' performance and it is simply a ratio of correctly predicted utterance to the total utterances.

$$Accuracy = \frac{Tr_{Po} + Tr_{Ne}}{Tr_{Po} + Fa_{Po} + Fa_{Ne} + Tr_{Ne}} \tag{15}$$

where Tr_{Po} represents truly positive cases that are accurately classified, Tr_{Ne} shows true negative cases are the negatives and also classy them into the negative category, Fa_{Po} terms as false positive that are negative cases but classified as positive elements and Fa_{Ne} values are false negative, which is positive identities while grouped into negatives. The standard deviation at sample level (STD.S) [36] is taken for the variation analysis of the performance measures. One cumulative performance parameter is proposed and defined using the standard predefined measures.

4.1.1 Weighted cumulation factor

The word cumulation is coined form the words (**Cumula**-tive+Aggrega-**tion**). The existing evaluation parameters cover one side and miss other aspects. To avoid this limitation we introduce a novel performance parameter aggregation that combinedly evaluated by three measures F_1 score - Dice coefficient - modified Hausdorff distance (FS-DC-MHD) cumulation. The FS-DC-MHD cumulation is computed by taking the unidirectional performance which means take the increasing or decreasing effects and termed as weighted cumulation factor (WCF). All the parameters are molded accordingly, as the high value of FS and DC is preferable, while the lower value of MHD is the first choice. The preferable MHD is of opposite nature hence we have taken the negative exponential of it in the parameter aggregation. The weight taken here for all cases is equal to 1. The value of WCF ranges from 0 to 1. For fully different sets, it is 0 and for similar matrices, it is 1.

$$WCF = FS.DG + DC.e^{-MHD} + e^{-MHD}.FS \tag{16}$$

4.2 Kernel size analysis

The central window diameter of the kernel is $R + 1$ for an even radius and R for odd one with all pixels of negative values. The outer layers of the kernel have positive values with smaller values near the central window to the outer region. The kernel and image can also be taken in the opposite way as for image $(Max(image) - image)$ and for the kernel just take the opposite sign and calculate all the results.

The Jaccard index value first increases with increasing the kernel radius as illustrated in Fig. 4a. At certain kernel radius with maximum Jaccard index, the performance decreases with an increase in radius. The ADL and Nuclei dataset images for spleen, kidney, and lung provide good performance for radius size $R = 5 - 8$ and for BreaKhis dataset $R = 6 - 10$ is the suitable range. Meanwhile, the time complexity observation with kernel radius is illustrated in Fig. 4b. BreaKhis dataset images show the high computational complexity and as compared to the ADL dataset images for low kernel radius. Initially, the average complexity increases rapidly with an increase in the kernel radius and then gradually. By analyzing the time complexity and the Jaccard index we performed an experiment for all the images at kernel radius $R = 6$.

4.3 Complex structure analysis

The segmentation performance at complex boundaries is depicted in Fig. 5. A larger set of visual results for multiple dataset images is given in the supplementary material. The average performance on all six datasets is considered for the evaluation of the proposed method.

The touching nuclei are shown inside cyan-colored ellipse and on the right side in the big rectangle in Fig. 5b. The touching nuclei are easily marked separately in Fig. 5c, using a suitable ellipse fitting. Meanwhile for the overlapped nuclei cases as shown inside the cyan circle, a small rectangle of red color, and left side in the big cyan rectangle. The overlapped nuclei are also tried to represent with their best-estimated boundary through the ellipse fitment method. Minimum 6 base points coordinates are required to plot an ellipsoidal but we have used 50 points to show the continuous curve of a nucleus as depicted in Fig. 5c.

4.4 Evaluation

The results are evaluated on the basis of qualitative and quantitative performance.

4.4.1 Qualitative evaluation

The visual illustration for the segmented sample images by different segmentation techniques as the BFC [62], SAM [55], FRFCM [37], MDRAN [54], LVMAC [45], PABVS

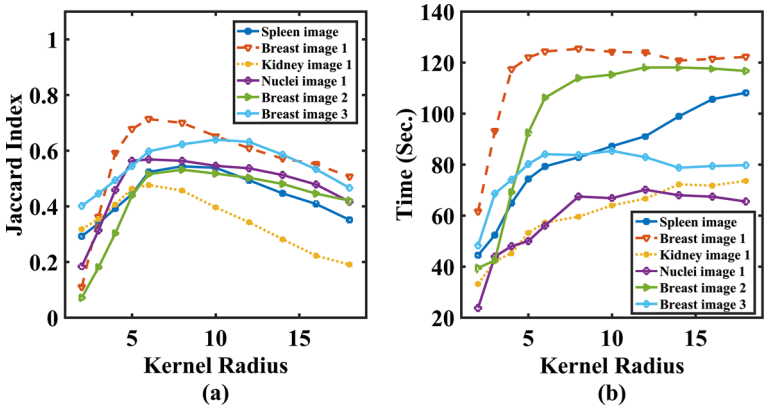

Fig. 4 The Jaccard index values are high for the kernel radius in the range of 5-12 **a** The Jaccard index versus kernel radius plot. **b** The plot for time analysis with variation in kernel radius for six different images. The taken to segment the image increases with an increase in kernel radius

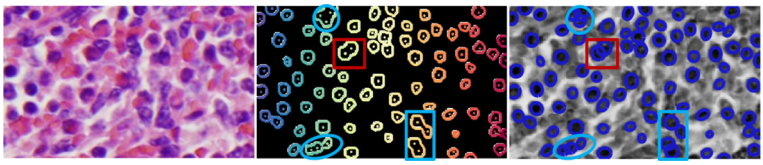

Fig. 5 Sample Illustration of histopathology image segmentation, **a** Original image **b** The nuclei centers and there associated boundaries **c** The suitable ellipse fitting for touching and overlapped nuclei

[61], FCMRG [46], and HCRF [53] comparison with the proposed method is depicted in Fig. 6. The segmentation outcome is illustrated through two samples $H\&E$ stained color images. The performance can be observed by the visual inspection of column-wise the result from the BFC method in the second column and the SAM method results in the third column in the upper part of the figure. The fourth and fifth columns show the results for MDRAN and LVMAC methods. The lower part of Fig. 6 from first, second, and third columns depict the segmentation results of PABVs, FCMRG, and HCRF methods, respectively. The lower

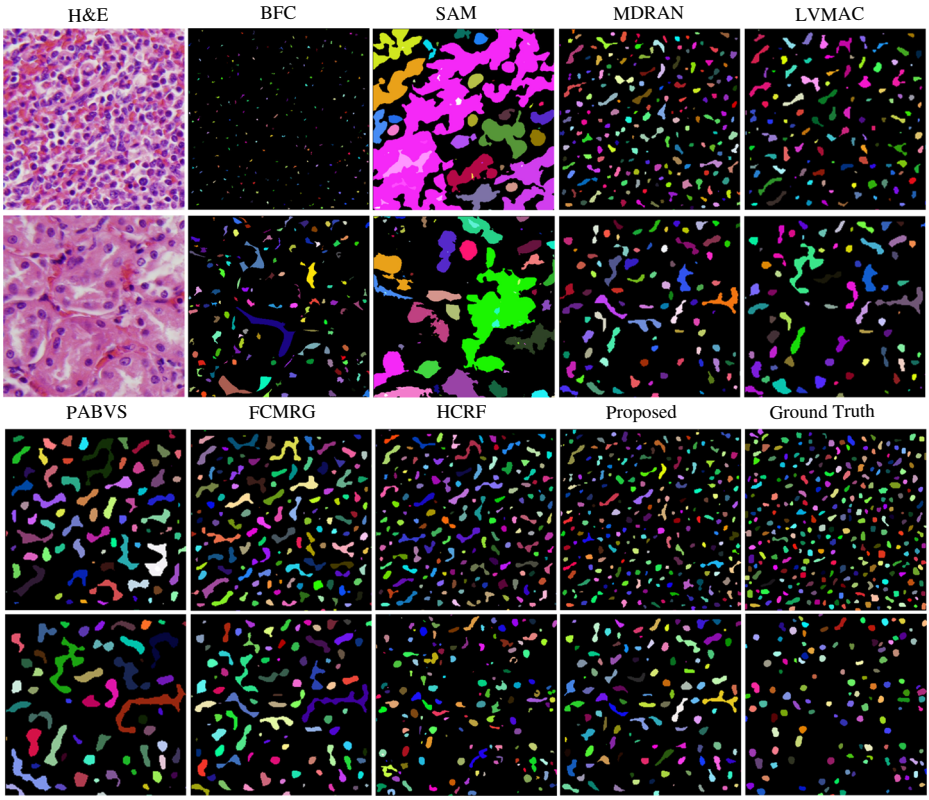

Fig. 6 Segmentation result illustration by two samples of H&E stained histopathology images ($400 \times 400 \times 3$) by the BFC, SAM, FRFCM, MDRAN, LVMAC, PABVS, FCMRG, HCRF, and proposed methods along with ground truth

Table 1 The comparison of FS of the proposed technique with state of the art methods for five different datasets

Dataset	BFC	SAM	FRFCM	MDRAN	LVMAC	PABVS	FCMRG	HCRF	Proposed
ADL	0.709	0.655	0.726	0.829	0.802	0.7931	0.685	0.854	0.916
Bisque	0.709	0.631	0.706	0.713	0.686	0.762	0.72	0.778	0.828
BreaKhis	0.593	0.586	0.558	0.741	0.714	0.85	0.769	0.877	0.934
Nuclei	0.621	0.778	0.66	0.829	0.802	0.762	0.836	0.903	0.938
MICCAI	0.709	0.655	0.726	0.818	0.791	0.871	0.799	0.854	0.916
Avg	0.668	0.661	0.675	0.786	0.759	0.808	0.762	0.853	0.906
STD.S	0.057	0.071	0.071	0.055	0.055	0.050	0.060	0.047	0.045

fourth and fifth columns in Fig. 6, depict the results of the proposed method and ground truth (GT), respectively.

4.4.2 Quantitative evaluation

The quantitative evaluation in terms of average FS for ADL, Bisque, BreaKhis, Nuclei, and MICCAI dataset are shown in Table 1. The BFC, SAM, and FRFCM methods show average FS (Mean±STD.S) 0.668±0.057, 0.661±0.071, and 0.675±0.071, respectively. The MDRAN, LVMAC, and PABVS methods gave 0.786±0.055, 0.759±0.055, and 0.808±0.050, respectively. The average FS by the FCMRG method is 0.762±0.060, and the HCRF approach provides 0.853±0.047 while the proposed algorithm offered 0.916±0.045 which is at least 6% better to all the baseline methods.

The DC analysis for all the considered datasets is discussed in Table 2. The BFC method offers maximum DC value for the Nuclei dataset 0.621 and the average value is 0.502± 0.065. The SAM, FRFCM, MDRAN, and LVMAC algorithms provide average DC 0.605± 0.039, 0.439± 0.050, 0.604± 0.030, and 0.701± 0.040, respectively. The PABVS, FCMRG, and HCRF methods gave average DC 0.607± 0.067, 0.681± 0.046, and 0.739± 0.021, respectively. The proposed method offered average DC 0.771± 0.016, which is at least or nearly 5% better as compared with state of art approaches.

Table 3 shows the comparative performance on all considered datasets of different methods with the proposed approach. The average MHD by the thee BFC method is 7.323±

Table 2 Analysis of Dice's coefficient for different state of the art methods with proposed method on five different datasets

Dataset	BFC	SAM	FRFCM	MDRAN	LVMAC	PABVS	FCMRG	HCRF	Proposed
ADL	0.469	0.657	0.477	0.605	0.63	0.585	0.727	0.746	0.782
Bisque	0.513	0.587	0.379	0.612	0.708	0.592	0.62	0.715	0.746
BreaKhis	0.611	0.636	0.389	0.577	0.725	0.576	0.659	0.723	0.778
Nuclei	0.45	0.567	0.473	0.577	0.712	0.557	0.674	0.767	0.765
MICCAI	0.469	0.577	0.477	0.65	0.728	0.725	0.725	0.746	0.783
Avg	0.502	0.605	0.439	0.604	0.701	0.607	0.681	0.739	0.771
STD.S	0.065	0.039	0.050	0.030	0.040	0.067	0.046	0.021	0.016

Table 3 MHD analysis of the proposed segmentation approach with state of the art methods for five different datasets

Dataset	BFC	SAM	FRFCM	MDRAN	LVMAC	PABVS	FCMRG	HCRF	Proposed
ADL	7.073	9.759	7.071	8.288	7.013	7.268	7.46	6.768	5.186
Bisque	5.287	12.273	6.274	7.295	7.891	9.275	8.303	6.707	4.903
BreaKhis	9.538	10.058	7.292	9.26	8.388	8.058	7.342	7.553	5.929
Nuclei	7.646	11.482	8.212	8.26	7.388	7.24	9.342	6.723	5.242
MICCAI	7.073	9.759	7.071	7.333	9.411	7.408	7.408	6.768	5.186
Avg	7.323	10.666	7.184	8.087	8.018	7.850	7.971	6.904	5.289
STD.S	1.523	1.147	0.693	0.813	0.935	0.863	0.861	0.364	0.381

1.523 (Mean±STD.S). The SAM, FRFCM, and MDRAN methods offered 10.666± 1.147, 7.184± 0.693, and 8.087± 8.813, respectively. The LVMAC, PABVS, FCMRG, and HCRF methods provided 8.018± 0.935, 7.850± 0.863, 7.971± 0.861, and 6.904± 0.364, respectively. The proposed segmentation method gave average MHD value 5.289± 0.381, which is at least 23% improvement than all the considered approaches for comparison.

The accuracy measure of the proposed technique is compared with mentioned state of art segmentation techniques like BFC [62], SAM [55], FRFCM [37], MDRAN [54], LVMAC [45], PABVS [61], FCMRG [46], and HCRF [53] for five different datasets is given in Table 4. The BFC method shows 0.729 accuracy for ADL dataset with 0.701± 0.033 (Mean±STD.S) average value. The SAM method shows 0.725 accuracy for Bisque dataset and its average accuracy performance is 0.687± 0.030. The FRFCM, MDRAN, and LVMAC methods segments the nuclei region with average accuracy 0.601± 0.102, 0.772± 0.010, and 0.837± 0.005, respectively. The FCMRG and HCRF methods provdes average accuracy 0.828± 0.017 and 0.868± 0.015, respectively. The proposed method gave the average accuracy of 0.927± 0.014, which is at least 7% greater than all state of the art methods.

4.5 Evaluation using WCF

The box plot [63] for the illustration of average performance using the weighted cumulation factor is shown in Fig. 7.

Table 4 Dadaset-wise accuracy analysis of the proposed segmentation system with different state of the art methods

Dataset	BFC	SAM	FRFCM	MDRAN	LVMAC	PABVS	FCMRG	HCRF	Proposed
ADL	0.729	0.695	0.655	0.785	0.843	0.825	0.817	0.884	0.926
Bisque	0.692	0.725	0.696	0.760	0.838	0.837	0.843	0.856	0.944
BreaKhis	0.729	0.697	0.47	0.773	0.829	0.814	0.822	0.877	0.918
Nuclei	0.65	0.674	0.512	0.763	0.838	0.836	0.850	0.847	0.937
MICCAI	0.707	0.643	0.671	0.779	0.837	0.817	0.810	0.875	0.909
Avg	0.701	0.687	0.601	0.772	0.837	0.826	0.828	0.868	0.927
STD.S	0.033	0.030	0.102	0.010	0.005	0.010	0.017	0.015	0.014

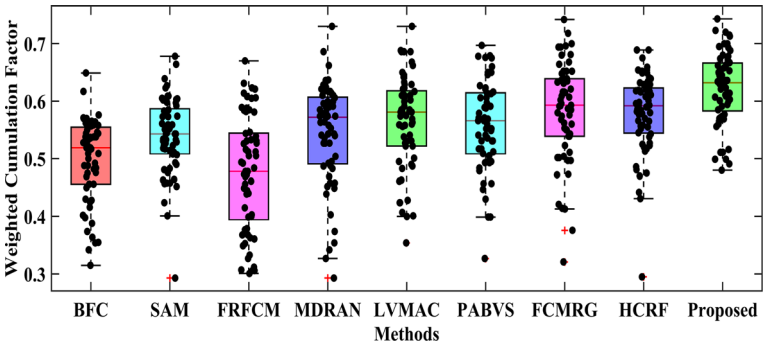

Fig. 7 The box plots illustrate the overall analysis of different methods on the test database using the weighted cumulation factor. The black dots represent the scores obtained for all 60 images by respective methods

The box has the centerline with median value within the box is overall best for the proposed method. The WCF for all the images is depicted by the black dots in the box plot along with the box (box shows two quartile 25%-75%) with median value as a horizontal line inside the box. The average value of WCF in the box plot for BC, SAM, and FRFCM methods is 0.482, 0.520, and 0.460, respectively. The MDRAN, LVMAC, and PABVS segmentation approach offered average WCF 0.525, 0.545, and 0.538, respectively. The FCMRG and HCRF methods gave 0.576 and 0.581, respectively, on the other hand, the proposed algorithm offered average WCF 0.623 which is at least 7% better as compared with all state of the art algorithms (Table 5).

4.6 Complexity analysis

The computational complexity of particular processing steps discussed at various subsections is given as exact computations required. Here we approximate the complexity and the worst-case computing complication is taken as the complexity of the algorithms. The BFC, SAM, and FRFCM methods have $O(N^3)$ computation complications. The MDRAN, PABVS, and HCRF algorithms offer the complexity of $O(N^4)$ while the LVMAC

Table 5 Complexity analysis of different image segmentation techniques

Method name and reference number	Complexity in order of N
SAM [55]	$O(N^3)$
BFC [62]	$O(N^3)$
FRFCM [37]	$O(N^3)$
MDRAN [54]	$O(N^4)$
LVMAC [45]	$O(N^{3.5})$
PABVS [61]	$O(N^4)$
FCMRG [46]	$O(N^{3.5})$
HCRF [53]	$O(N^4)$
Proposed method	$O(N^3)$

and FCMRG proffer $O(N^{3.5})$ computational operations. The proposed method offers the computing complexity of $O(N^3)$.

5 Conclusion

A novel content-based histopathology image segmentation method using a multi radial kernel has been proposed in this manuscript. It is a three-stage method where histogram equalization and multi radial circular kernel are used for pre-processing followed by B-spline function based nuclei center and region extraction and finally center to boundary association and curve fitting are applied for complete nuclei segmentation. The performance of the segmentation technique is evaluated in terms of average FS, Dice coefficient, and modified Hausdorff distance, and a novel introduced parameter weighted cumulation factor (WCF) to define overall performance. In evaluation with existing state of art methods, proposed method is showing at least 6%, 23% and 7% improvement in FS, modified Hausdorff distance, and WCF respectively. The process can further be used for grading of the disease using various classifiers. This method may also be employed for the segmentation of objects of different sizes and shapes in various applications.

Acknowledgment Thanks to Dr. Neelkamal Kapoor (professor and head) and Dr. Deepti Joshi (Pathologist) from pathology Dept., AIIMS, Bhopal, India, and Dr. Pradeep Kolekar (Medical Director) JNCH&RC Bhopal, India, for giving guidance and backing in dataset construction and annotation of ground truth.

References

1. Al-Kofahi Y, Lassoued W, Lee W, Roysam B (2010) Improved automatic detection and segmentation of cell nuclei in histopathology images. IEEE Trans Biomed Eng 57(4):841–852
2. Ali S, Madabhushi A (2012) An integrated region-, boundary-, shape-based active contour for multiple object overlap resolution in histological imagery. IEEE Trans Med Imaging 31(7):1448–1460
3. Bernard O, Friboulet D, Thevenaz P, Unser M (2009) Variational b-spline level-set: a linear filtering approach for fast deformable model evolution. IEEE Trans Image Process 18(6):1179–1191
4. Canny J (1986) A computational approach to edge detection. IEEE Trans Pattern Anal Mach Intell PAMI-8(6):679–698
5. Chan TF, Vese LA (2001) Active contours without edges. IEEE Trans Image Process 10(2):266–277
6. Chang H, Han J, Borowsky A, Loss L, Gray JW, Spellman PT, Parvin B (2013) Invariant delineation of nuclear architecture in glioblastoma multiforme for clinical and molecular association. IEEE Trans Med Imaging 32(4):670–682
7. Chowdhary C (2015) Decrease in false assumption for detection using digital mammography. 12
8. Chowdhary C, Acharjya D (2016) A hybrid scheme for breast cancer detection using intuitionistic fuzzy rough set technique. Int J Healthc Inf Syst Inform (IJHISI) 11(2):38–61
9. Chowdhary C, Acharjya D (2017) Clustering algorithm in possibilistic exponential fuzzy c-mean segmenting medical images. J Biomimetics Biomater Biomed Eng 30:12–23, 02
10. Chowdhary C, Acharjya D (2017) Clustering algorithm in possibilistic exponential fuzzy c-mean segmenting medical images. J Biomimetics Biomater Biomed Eng 30:12–23, 2
11. Chowdhary C, Acharjya D (2018) Segmentation of mammograms using a novel intuitionistic possibilistic fuzzy c-mean clustering algorithm. 01:75–82
12. Chowdhary C, Acharjya D (2020) Segmentation and feature extraction in medical imaging: a systematic review. Procedia Comput Sci 167:26–36. International Conference on Computational Intelligence and Data Science
13. Dice LR (1945) Measures of the amount of ecologic association between species. Ecology
14. Dubuisson M, Jain AK (1994) A modified hausdorff distance for object matching. In: Proceedings of 12th international conference on pattern recognition, vol 1, pp 566–568

15. Dundar MM, Badve S, Bilgin G, Raykar V, Jain R, Sertel O, Gurcan MN (2011) Computerized classification of intraductal breast lesions using histopathological images. IEEE Trans Biomed Eng 58(7):1977–1984
16. Fatakdawala H, Xu J, Basavanhally A, Bhanot G, Ganesan S, Feldman M, Tomaszewski JE, Madabhushi A (2010) Expectation–maximization-driven geodesic active contour with overlap resolution (emagacor): Application to lymphocyte segmentation on breast cancer histopathology. IEEE Trans Biomed Eng 57(7):1676–1689
17. Fitzgibbon A, Pilu M, Fisher RB (1999) Direct least square fitting of ellipses. IEEE Trans Pattern Anal Mach Intell 21(5):476–480
18. Gu Y, Chanussot J, Jia X, Benediktsson JA (2017) Multiple kernel learning for hyperspectral image classification: a review. IEEE Trans Geosci Remote Sens 55(11):6547–6565
19. Hanbury AG, Serra J (2001) Morphological operators on the unit circle. IEEE Trans Image Process 10(12):1842–1850
20. Haralick RM, Zhuang X, Lin C, Lee JSJ (1989) The digital morphological sampling theorem. IEEE Trans Acoust Speech Signal Process 37(12):2067–2090
21. Heijmans HJAM (1991) Theoretical aspects of gray-level morphology. IEEE Trans Pattern Anal Mach Intell 13(6):568–582
22. Irshad H, Veillard A, Roux L, Racoceanu D (2014) Methods for nuclei detection, segmentation, and classification in digital histopathology: a review—current status and future potential. IEEE Rev Biomed Eng 7:97–114
23. Ishii S, Lee S, Urakubo H, Kume H, Kasai H (2020) Generative and discriminative model-based approaches to microscopic image restoration and segmentation. Microscopy 69(2):79–91, 03
24. Janowczyk A, Doyle S, Gilmore H, Madabhushi A (2018) A resolution adaptive deep hierarchical (radhical) learning scheme applied to nuclear segmentation of digital pathology images. Comput Methods Biomech Biomed Eng Imaging Vis 6(3):270–276
25. Jiu M, Sahbi H (2017) Nonlinear deep kernel learning for image annotation. IEEE Trans Image Process 26(4):1820–1832
26. Jiu M, Sahbi H (2017) Nonlinear deep kernel learning for image annotation. IEEE Trans Image Process 26(4):1820–1832
27. Kauser Ahmed P, Acharjya D (2019) A hybrid scheme for heart disease diagnosis using rough set and cuckoo search technique. J Med Syst 12:27
28. Khayam SA (2003) The discrete cosine transform (dct): Theory and application. Department of electrical and computing engineering
29. Kim W, Kanezaki A, Tanaka M (2020) Unsupervised learning of image segmentation based on differentiable feature clustering. IEEE Trans Image Process 29:8055–8068
30. Kresch R, Malah D (1998) Skeleton-based morphological coding of binary images. IEEE Trans Image Process 7(10):1387–1399
31. Kumar N, Verma R, Sharma S, Bhargava S, Vahadane A, Sethi A (2017) A dataset and a technique for generalized nuclear segmentation for computational pathology. IEEE Trans Medical Imaging 36(7):1550–1560
32. Kurmi Y, Chaurasia V (2018) Multifeature-based medical image segmentation. IET Image Process 12(8):1491–1498
33. Kurmi Y, Chaurasia V (2020) Classification of magnetic resonance images for brain tumor detection. IET Image Process 4:1–13
34. Kurmi Y, Chaurasia V, Ganesh N (2019) Tumor malignancy detection using histopathology imaging. J Med Imaging Radiat Sci 50(4):514–528
35. Kurmi Y, Chaurasia V, Goel A, Joshi D, Kapoor N (2020) Tuberculosis bacteria analysis in acid fast stained images of sputum smear. Signal Image Vid Process 03
36. Kurmi Y, Chaurasia V, Kapoor N (2020) Design of a histopathology image segmentation algorithm for cad of cancer. Optik 218:164636
37. Lei T, Jia X, Zhang Y, He L, Meng H, Nandi AK (2018) Significantly fast and robust fuzzy c-means clustering algorithm based on morphological reconstruction and membership filtering. IEEE Trans Fuzzy Syst 26(5):3027–3041
38. Lei W, Lin Y (2020) A novel dynamic fingerprint segmentation method based on fuzzy c-means and genetic algorithm. IEEE Access 8:132,694–132,702
39. Li X, Plataniotis KN (2015) A complete color normalization approach to histopathology images using color cues computed from saturation-weighted statistics. IEEE Trans Biomed Eng 62(7): 1862–1873
40. Liang J, Zhang M, Liu D, Zeng X, Ojowu O, Zhao K, Li Z, Liu H (2013) Robust ellipse fitting based on sparse combination of data points. IEEE Trans Image Process 22(6):2207–2218

41. McCann MT, Mixon DG, Fickus MC, Castro CA, Ozolek JA, Kovacevic J (2014) Images as occlusions of textures: a framework for segmentation. IEEE Trans Image Process 23(5):2033–2046
42. Mújica-Vargas D, Kinani JM, Rubio JdJ (2020) Color-based image segmentation by means of a robust intuitionistic fuzzy c-means algorithm. Int J Fuzzy Syst 22:901–916, 03
43. Nameirakpam D, Chanu Y (2020) An image segmentation approach based on fuzzy c-means and dynamic particle swarm optimization algorithm. Multimed Tools Appl 03
44. Otsu N (1979) A threshold selection method from gray-level histograms. IEEE Trans Syst Man Cybern 9(1):62–66
45. Peng Y, Liu S, Qiang Y, Wu X, Hong L (2019) A local mean and variance active contour model for biomedical image segmentation. J Comput Sci 33:11–19
46. Sheela C, Suganthi G (2020) Morphological edge detection and brain tumor segmentation in magnetic resonance (mr) images based on region growing and performance evaluation of modified fuzzy c-means (fcm) algorithm. Multimed Tools Appl 02
47. Sirinukunwattana K, Snead DRJ, Rajpoot N (2015) A stochastic polygons model for glandular structures in colon histology images. IEEE Trans Med Imaging 34(11):2366–2378
48. Song J, Xiao L, Lian Z (2017) Boundary-to-marker evidence-controlled segmentation and mdl-based contour inference for overlapping nuclei. IEEE J Biomed Health Inf 21(2):451–464
49. Song J, Xiao L, Lian Z (2018) Contour-seed pairs learning-based framework for simultaneously detecting and segmenting various overlapping cells/nuclei in microscopy images. IEEE Trans Image Process 27(12):5759–5774
50. Spanhol FA, Oliveira LS, Petitjean C, Heutte L (2016) A dataset for breast cancer histopathological image classification. IEEE Trans Biomed Eng 63(7):1455–1462
51. Srinivas U, Mousavi HS, Monga V, Hattel A, Jayarao B (2014) Simultaneous sparsity model for histopathological image representation and classification. IEEE Trans Med Imaging 33(5):1163–1179
52. Su H, Xing F, Yang L (2016) Robust cell detection of histopathological brain tumor images using sparse reconstruction and adaptive dictionary selection. IEEE Trans Med Imaging 35(6):1575–1586
53. Sun C, Li C, Zhang J, Ai S, Chen H, Kulwa F, Li X, Jiang T (2020), Gastric histopathology image segmentation using a hierarchical conditional random field
54. Vu QD, Graham S, Kurc T, To MNN, Shaban M, Qaiser T, Koohbanani NA, Khurram SA, Kalpathy-Cramer J, Zhao T, Gupta R, Kwak JT, Rajpoot N, Saltz J, Farahani K (2019) Methods for segmentation and classification of digital microscopy tissue images. Front Bioeng Biotechnol 7:53
55. Wang Z (2016) A semi-automatic method for robust and efficient identification of neighboring muscle cells. Pattern Recogn 53:300–312
56. Wang H, Lu X, Hu Z, Zheng W (2014) Fisher discriminant analysis with l1-norm. IEEE Trans Cybern 44(6):828–842
57. Wang W, Ozolek JA, Slepcev D, Lee AB, Chen C, Rohde GK (2011) An optimal transportation approach for nuclear structure-based pathology. IEEE Trans Med Imaging 30(3):621–631
58. Xia J, Li X, Chen G, Zhang C (2020) A new hybrid brain mr image segmentation algorithm with super-resolution, spatial constraint-based clustering and fine tuning. IEEE Access 8:135,897–135,911
59. Xu Y, Zhu J, Chang E, Tu Z (2012) Multiple clustered instance learning for histopathology cancer image classification, segmentation and clustering. In: IEEE Conference on Computer Vision and Pattern Recognition, June, vol 2012, pp 964–971
60. Ye J, Wu P, Wang JZ, Li J (2017) Fast discrete distribution clustering using wasserstein barycenter with sparse support. IEEE Trans Signal Process 65(9):2317–2332
61. Yu C, Yan Y, Zhao S, Zhang Y (2020) Pyramid feature adaptation for semi-supervised cardiac bi-ventricle segmentation. Comput Med Imaging Graph 81:101697
62. Zafari S, Eerola T, Sampo J, Kälviäinen H, Haario H (2015) Segmentation of overlapping elliptical objects in silhouette images. IEEE Trans Image Process 24(12):5942–5952
63. Zerovnik J, Rupnik Poklukar D (2017) Elementary methods for computation of quartiles. Teach Stat 39(3)
64. Zhao H (2020) An image segmentation approach on improved implicit surface model in straddle strategy. Multimed Tools Appl 02